Shock Ignition Laser-Plasma Interactions in Ignition-Scale Plasmas

R. H. H. Scott,[1,*] K. Glize,[1] L. Antonelli,[2] M. Khan,[2] W. Theobald,[3] M. Wei,[3] R. Betti,[3] C. Stoeckl,[3] A. G. Seaton,[4] T. D. Arber,[5] D. Barlow,[5] T. Goffrey,[5] K. Bennett,[5] W. Garbett,[6] S. Atzeni,[7] A. Casner,[8] D. Batani,[8] C. Li,[9] and N. Woolsey[2]

[1]*Central Laser Facility, STFC Rutherford Appleton Laboratory, Harwell Oxford, Oxfordshire OX11 OQX, United Kingdom*
[2]*York Plasma Institute, Department of Physics, University of York, York YO10 5DD, United Kingdom*
[3]*Laboratory for Laser Energetics, University of Rochester, Rochester, New York 14623-1299, USA*
[4]*Los Alamos National Laboratory, Los Alamos, New Mexico 87545, USA*
[5]*University of Warwick, Coventry CV4 7AL, United Kingdom*
[6]*AWE, Aldermaston, Reading, Berkshire RG7 4PR, United Kingdom*
[7]*Dipartimento SBAI, Università di Roma "La Sapienza", Roma 00161, Italy*
[8]*CELIA, University of Bordeaux, Bordeaux F-33405, France*
[9]*MIT, Cambridge, Massachusetts 02139, USA*

(Received 17 March 2021; revised 23 June 2021; accepted 2 July 2021; published 4 August 2021)

We use a subignition scale laser, the 30 kJ Omega, and a novel shallow-cone target to study laser-plasma interactions at the ablation-plasma density scale lengths and laser intensities anticipated for direct drive shock-ignition implosions at National Ignition Facility scale. Our results show that, under these conditions, the dominant instability is convective stimulated Raman scatter with experimental evidence of two plasmon decay (TPD) only when the density scale length is reduced. Particle-in-cell simulations indicate this is due to TPD being shifted to lower densities, removing the experimental back-scatter signature and reducing the hot-electron temperature. The experimental laser energy-coupling to hot electrons was found to be 1%–2.5%, with electron temperatures between 35 and 45 keV. Radiation-hydrodynamics simulations employing these hot-electron characteristics indicate that they should not preheat the fuel in MJ-scale shock ignition experiments.

DOI: 10.1103/PhysRevLett.127.065001

Laser inertial confinement fusion [1] uses a spherical implosion to integrate photon flux (laser light for direct drive, x rays for indirect drive) in space and time. Photon absorption heats the outer surface of a spherical shell containing the fusion fuel, creating an outward plasma flow, which, through conservation of momentum, drives the cold fuel inwards. The imploding fuel reduces in volume, causing an increase in pressure, this in turn decelerates the fuel, converting the fuel's kinetic energy into internal energy. This raises the temperature, compresses the fuel, and initiates fusion. In comparison to indirect drive, direct drive couples 5–6 [2] times more laser energy to implosion kinetic energy, potentially reducing the required laser energy by an equivalent factor. Direct drive is subject to higher Rayleigh-Taylor instability (RTI) growth [3,4] than indirect drive due to shorter ablation-front scale lengths and perturbations seeded by laser-intensity inhomogeneities.

Shock ignition [5] reduces the sensitivity to RTI by reducing the implosion velocity: rather than relying purely on the conversion of implosion kinetic energy to internal energy, a laser-driven shock initiates fusion burn. The shock occurs late in the implosion and, when timed correctly, collides with an outgoing shock emerging from the center of the target at the inner surface of the dense deuterium-tritium ice-gas interface. This collision amplifies the shock, which then propagates inwards through the compressed, yet subignition, gaseous hotspot, further heating the ions and compressing the hotspot and shell to initiate ignition. Radiation-hydrodynamic simulations indicate it may be possible to achieve ignition via shock ignition well within the energy-limits of National Ignition Facility (NIF) [6].

Laser direct drive central hotspot designs are typically restricted to laser intensities $\leq 1.3 \times 10^{15}$ W cm^{-2} due to the rapid growth of laser plasma instabilities (LPIs) above this intensity. In particular, two plasmon decay (TPD) and stimulated Raman scatter (SRS) can stimulate the growth of electron-plasma waves (EPWs) in the ablated plasma. The EPWs accelerate electrons to high energy; these can then penetrate and heat the target, reducing the fuel's compressibility, potentially preventing ignition. Furthermore, the EPWs and ion-acoustic waves (driven by stimulated Brillouin scatter, or SBS) can enhance reflectivity, reducing laser absorption. Cross-beam energy transfer (CBET) can further reduce absorption.

In order to launch a shock of sufficient strength for shock ignition, peak intensities that exceed the LPI thresholds [7] are needed, and can reach $\sim 1 \times 10^{16}$ W cm^{-2}. As a result, shock ignition is potentially susceptible to poor laser coupling and fuel preheat.

Previous work in the shock ignition intensity regime [8–21] indicates that the hot-electron temperature is in the range 20–60 keV, however, this work was not performed with both the intensity required for shock ignition, and in ablation plasma conditions closely resembling the long plasma length scales expected in a direct-drive ignition-scale implosion. Implosion density scale lengths are dictated by the target radius (due to plasma flow divergence), as well as laser intensity, energy, and pulse length. For example, Omega direct drive implosions have density scale lengths at the quarter critical density $(L_{n_c/4}) \sim 125$ μm and electron temperature $(T_e) \sim 2$ keV, while those from NIF 1.8 MJ direct drive ignition implosion simulations [22] are $L_{n_c/4} = 500 - 600$ μm and $T_e \sim 4$ keV. As the characteristics of LPIs are dependent on $L_{n_c/4}$, T_e and laser intensity [7], combined with the complexity of the kinetic processes driving LPIs, extrapolation from experiments at subignition scale lengths and temperatures to the ignition scale is not possible. This Letter describes the first laser-plasma interaction experiment performed at ignition scale and at laser intensities of relevance to shock ignition.

A novel target design was created in order to reproduce the anticipated ablation-plasma conditions for an ignition-scale laser direct drive implosion using a subignition facility. Planar targets effectively have an infinite radius of curvature and hence the potential for long density scale lengths. 20 of Omega's 60 beams can be coupled onto a planar target, these are arranged as cones with incidence angles of 23°, 48°, and 62°. 10 of these 20 beams (5 kJ) are used to create a long density scale-length ablation plasma, with the remaining 10 beams (5 kJ) driving a "shock ignition" pulse into this preformed ablation plasma. The 62° cone of beams have a high angle of incidence (θ) on target, this results in beam reflection at low density ($n_{\mathrm{refl}} = n_c \cos^2\theta$, where n_{refl} is the electron density where reflection occurs), resulting in inefficient laser absorption. Simulations indicate the absorption is as low as 60%, reducing the ablation rate, and forming short density scale lengths of ~200 μm.

Laser-target coupling is improved using a novel flat-tipped shallow-cone target and repointing the low-intensity laser beams past the cone axis of symmetry. The conical target has the effect of reducing the beams' effective angle of incidence θ, significantly improving the predicted absorption to 90%. A schematic of the target and example beam position is shown in Fig. 1(a). Furthermore, the conical geometry acts to reduce the divergence of the ablation plasma flow, this further increases the density scale length. Moreover, maintaining an open-cone geometry avoids plasma flow convergence on axis and jet formation. Simulations used the two-dimensional (2D), cylindrically symmetric Lagrangian radiation-hydrodynamics code H2D [23], with 3D laser ray tracing, SESAME equations of state [24], multigroup diffusive radiation transport, and flux-limited thermal conductivity. The optimal laser

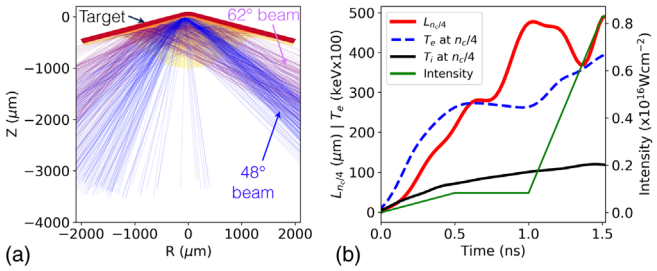

FIG. 1. (a) The open-cone target design employed to generate large ablation-plasma scale lengths, shown just before the high-intensity beams switch on at 1.0 ns. Only two low-intensity beams are shown for clarity. (b) Simulated density scale length, electron temperature, and intensity at $n_c/4$ as a function of time using the open-cone target.

configuration for maximizing density scale length with the conical target is set out in Table I. The calculated $L_{n_c/4}$ and T_e at the quarter-critical surface are shown in Fig. 1(b), and predict ignition-scale density scale lengths of 450 μm and T_e 3 keV at 1 ns; the time at which the high-intensity interaction commences.

The target (Fig. 1) comprised a 3.6 mm diameter cone of 152° opening angle with a 100 μm diameter flat tip. The laser was incident on a 40 μm thick CH plastic ablator, backed with a 5 μm copper (Cu) diagnostic layer, followed by 30 μm of CH to tamp target expansion and prevent electron refluxing. By varying the power in the high-intensity beams on a given shot, a range of peak intensities, corrected for inverse bremsstrahlung absorption, from 8×10^{14} to 8.3×10^{15} W cm^{-2} were incident on the $n_c/4$ surface, which based on simulations, was located ~200 μm from the target front surface. The nominal delay between low and high intensity beams was 1 ns. A total of 12 target shots were performed.

Laser-light backscattered into two of the high-intensity beams on the 23° beam cone was temporally and spectrally resolved using the full aperture back-scatter (FABS) diagnostic. Backscattered light not entering the beam port was imaged using the near back-scatter imager (NBI) and filtered to distinguish SBS (~351 nm) and SRS and/or TPD (400–700 nm) components. Hot electron production was diagnosed from Cu K-shell line emission using an absolutely calibrated Zinc von Hamos spectrometer (ZVH [25]) across the spectral region 8–9 keV and a spherically bent quartz crystal imager (SCI [26]) aligned to the Cu K_α spectral line at 8047.8 eV. The SCI has a narrow spectral window of 8047–8054 eV and recorded data onto an image plate (IP). The hot-electron temperature was inferred from bremsstrahlung emission using a nine-channel, differentially filtered IP based time-integrated hard x-ray diagnostic (HXIP [27]) over the range 10–200 keV.

Figure 2(a) is an example of the backscattered light spectra with a ~450 μm density scale length. The early-time (< 1 ns) back-scatter signal is attributed to TPD: the

TABLE I. Optimized beam configuration for creating large scale-length ablation plasmas on Omega. Intensities are the total for that cone with SSD off: SSD on ~0.87 × SSD off.

Beam-cone angle (°)	Phase plate	No. beams	Energy (J)	Pointing (μm)		Intensity (W cm^{-2})
				R	Z	
23	IDI300	5	≤ 500	0	−200	5.3e15
62	IDI300	5	≤ 500	0	−200	3.0e15
48	SG5	5	500	0	0	4.6e14
62	SG5	5	500	0	−300	3.7e14

narrow-band spectral features above and below 702 nm have previously been shown to be indicative of TPD [28,29]. As the high-intensity beams ramp up after 1 ns, a broad, bright spectral feature is seen across the 475–600 nm range. This broad feature is consistent with backscattered light caused by convective SRS [30]: the backscattered light originates from densities in the range $0.04 - 0.16 n_c$—well below the ~0.22–0.25n_c range where TPD is able to occur [29]. The white dashed line indicates the normalized SRS threshold (I_{thSRS}) assuming a linear density profile [7,31] $I_{\mathrm{thSRS}}(\mathrm{W\,cm^{-2}}) = 4 \times 10^{17}/L_{n_c/4}\ (\mu\mathrm{m})\,\lambda\,(\mu\mathrm{m})$, where λ is the laser wavelength. I_{thSRS} is normalized using the calculated $n_c/4$ intensity with as-shot powers. This was found to consistently predict the onset of convective SRS. SRS reflectivity measured in one high-intensity beam port (B25) as a function of single-beam intensity is shown in Fig. 3(b). During the high-intensity part of the drive, no clear evidence of TPD nor absolute SRS was observed. The sharp cutoff in signal below ~480 nm is not unexpected as the lower densities reduce convective SRS gain and enhance Landau damping, however, it may also be a signature of SRS rescatter [32].

Bremsstrahlung radiation emission produced through the collision of hot electrons within the target enables estimation of the hot-electron temperature. Measurements from the time-integrated HXIP instrument are interpreted using a GEANT4-derived instrument response function [33] and χ^2 minimization techniques. Any low-energy x rays from the ablation plasma and/or Cu K-shell emission were removed by excluding the two lower-energy HXIP channels. The inferred hot-electron temperatures are in the range ~35–45 keV, as shown by the red points in Fig. 3(a).

The fraction of total laser energy converted to hot electrons was inferred from the K_α yield, as measured using the ZVH diagnostic. The number of K_α photons was extracted from background-subtracted ZVH data and then converted into hot-electron energy using GEANT4 Monte Carlo simulations [34] that use the cold target geometry and a 40 keV Maxwellian hot-electron population. A conversion efficiency of between 1% and 2.5% [green points in Fig. 3(a)] is inferred, with some suggestion of an intensity dependence. Modeling indicates laser ablation-induced x-ray emission did not contribute to the signal. These data are consistent with SCI K_α images.

When only low intensity beams interact with the target it is interesting to note that the SCI data are smooth, as illustrated in Fig. 4(a). On adding the high intensity beams, small-scale structures were visible [Fig. 4(b)]. These structures with ~75 μm FWHM are slightly smaller than that of the vacuum focus (105 × 144 μm) of the high-intensity beams. Comparison of FABS data with and without the high-intensity beams indicates these structures are correlated with SRS-generated hot electrons. The small spatial scale of these structures is suggestive of limited divergence of these hot electrons, however, it is not possible to quantify this with the available data.

A comparison measurement at shorter density scale lengths is possible by reducing the delay of the high-intensity beams with respect to the low-intensity beams to 0.7 ns. This limits the plasma expansion duration, reducing the quarter-critical density scale length to ~300 μm [see Fig. 1(b)]. An alternative is to switch to a planar target, this further reduces the density scale length to ~200 μm. Radiation-hydrodynamic simulations predict a reduction

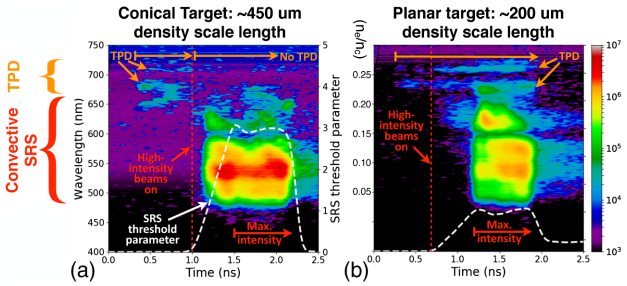

FIG. 2. FABS steaked back-scatter spectra: (a) Typical long density scale-length data: TPD is visible at early time, while during the high-intensity pulse convective SRS dominates. (b) Reduced density scale length with a planar target: TPD is visible throughout. In both cases, the low intensity beams ramp up from 0–0.5 ns, while the maximum intensity is 8.5×10^{15} W cm^{-2}. Y axes and color scale apply to both plots, with densities assuming a temperature of 3 keV. White dashed lines indicate the SRS threshold parameter (> 1 is above threshold), red dashed line indicates the point at which the high intensity beams turn on. In the small density scale length case (where SRS is just above threshold) TPD is visible throughout. This is not the case in the long scale length when SRS is well above threshold. The FABS data were highly reproducible.

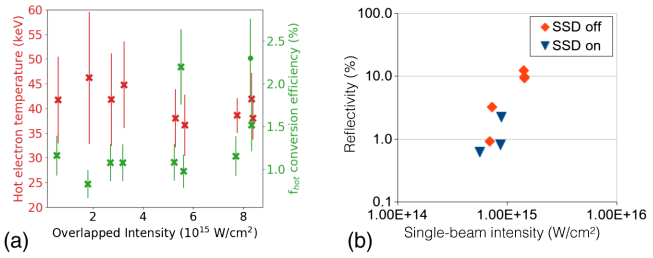

FIG. 3. (a) Hot-electron temperature and total laser energy conversion to hot electrons as a function of intensity. (b) SRS reflectivity from (high-intensity) beam 25.

in the electron temperature to 2.5 and 2 keV, respectively, for these two cases. At the shortest density scale length [see Fig. 2(b)] TPD is visible throughout the interaction during the low intensity and high intensity parts of the laser pulse. Moreover, SRS is just above threshold during the high-intensity interaction. This contrasts with the long scale length case, where TPD is not observed and the high intensity interaction significantly exceeds the SRS threshold. This suggests a transition from a small scale-length TPD-dominated regime, to a long scale-length regime which appears to be dominated by convective SRS.

To investigate the relative roles of TPD and convective SRS in these experiments, 2D plane-wave EPOCH [35] PIC simulations were performed [36] in a density scale length, electron (ion) temperature and intensity regime of direct relevance to this experiment: $0.1-0.26n_c$, 600 μm, 4.5 (2.25) keV, and 2×10^{15} W cm^{-2}, respectively. These simulations show qualitative agreement with the experiments. Figure 5(a) shows the transverse wave number (k_y) spectrum of the electron plasma waves (EPWs) at 22.5 ps. The EPWs are principally in the region $0.19-0.24n_c$. However, examination of the time-averaged reflected light spectrum in Fig. 5(b) [which shows qualitative agreement with Fig. 2(a)] indicates that there is little emission from $0.2-0.24n_c$. Detailed examination of k_xk_y k-space plots of restricted spatial extent (not shown) reveals that the EPWs in the region from $0.20-0.24n_c$ are principally caused by TPD—explaining the lack of reflected light emitted from this region, and providing a compelling explanation for the "Raman Gap" [37]. The occurrence of TPD at these densities is attributed to convective TPD [38]. The low

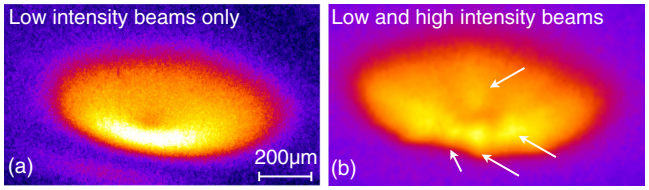

FIG. 4. (a) SCI image with low-intensity beams only; the deposition profile is smooth. (b) SCI image with low and high-intensity beams exhibiting small-scale structures (highlighted with white arrows).

(32 keV) hot-electron temperature in the simulations—in approximate agreement with experiments—is ascribed to the fact that EPW phase velocities increase rapidly as n_e approaches $n_c/4$: as the EPW wave spectrum, which is comprised of TPD EPWs and low-density SRS EPWs, is shifted below $n_c/4$, this limits EPW phase velocities, and hence the hot-electron temperature. At the simulated intensity, convective SRS is just above threshold, therefore at higher intensities it would be expected for pump depletion due to convective SRS at lower densities to play an increasing role in governing the competition between TPD and SRS [39]. Nevertheless, we have shown that a significant factor in the dynamics observed experimentally and via simulation is likely explained by the shifting of TPD to lower densities, thereby removing the experimental $\omega_0/2$ "doublet" diagnostic feature, preventing convective SRS backscatter from ~0.20–$0.24n_c$, and reducing the hot-electron temperature.

To assess the impact of the hot electrons observed in these experiments on an implosion, 2D Arbitrary Lagrangian Eulerian radiation-hydrodynamics simulations were performed of a 500 kJ shock-ignition implosion [40] using ODIN [41]. During the laser ray-trace, energy is extracted from the laser (2.5%) and hot electrons are launched from the $n_c/4$ surface with a 40 keV temperature, in a 45° cone. A Monte Carlo approach (bench-marked against MCNP [42]) is used for hot-electron transport, scattering, and energy deposition. Using these experimentally measured hot-electron characteristics, Fig. 6(a) shows the pressure generated is unaffected by the hot electrons, while Fig. 6(b) shows very little degradation in the density profile; an encouraging result for future MJ-scale shock-ignition experiments.

In summary, using a novel target design fielded on the 30 kJ Omega laser facility, we have found that in ablation plasma conditions of relevance to shock ignition at 1.8 MJ scale and intensities up to 8.5×10^{15} W cm^{-2}, the hot-electron temperature remains relatively low at 35–45 keV,

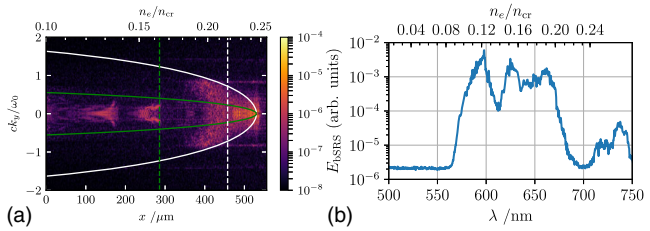

FIG. 5. (a) Spatially resolved (averaged in Y) transverse wave number (k_y) spectrum of the EPWs' electrostatic (E_x) fields at 22.5 ps. The solid (dashed) green line indicates the wave numbers required for SRS sidescatter (the density below which $k\lambda_{\mathrm{Debye}}\geq0.3$). The solid (dashed) white line indicates the curve of maximum-growth for TPD (Landau cutoff for TPD). (b) The back-scatter light spectrum extracted from PIC simulations from 20–25 ps.

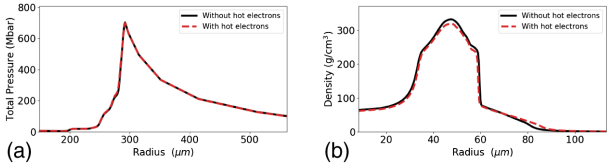

FIG. 6. Simulations with and without the experimentally measured hot-electron characteristics show no degradation: (a) pressures during the laser power spike, and (b) density at peak compression.

with up to ~2.5% of the laser energy converted to hot-electrons. While back-scatter diagnostics indicate the dominance of convective SRS, PIC simulations indicate both SRS and TPD are present, but TPD occurs at density $< n_c/4$, meaning the EPW phase velocities are reduced, explaining the relatively low observed hot-electron temperature in both experiments and simulations, and the absence of backscattered light from near $n_c/4$. Hydrosimulations indicate the low observed hot-electron number and temperature is compatible with shock-ignition at MJ scales. This new ability to study LPIs in ignition scale plasmas, but with significantly reduced laser energy, is an important development which could revolutionize LPI studies if implemented on future kJ-class, high repetition rate laser systems, by enabling the gathering of large, statistically significant, datasets which can be used to verify and reduce uncertainty in physics models.

In conclusion we have performed an initial evaluation of laser-plasma interactions in ablation plasma conditions of direct relevance to shock ignition at NIF scale. These initial results are promising for the pursuit of shock ignition at ignition scales.

This work was funded by EPSRC Grants No. EP/P023460/1, No. EP/P026486/1, and No. EP/P026486/1. This work has been carried out within the framework of the EUROfusion Consortium and has received funding from the EuroFUSION research and training programme under Grant Agreement No. 633053. The views and opinions expressed herein do not necessarily reflect those of the European Commission. The involved teams have operated within the framework of the Enabling Research Project: ENR-IFE19.CEA-01 Study of Direct Drive and Shock Ignition for IFE: Theory, Simulations, Experiments, Diagnostics development.

*Robbie.Scott@stfc.ac.uk

[1] J. Nuckolls, L. Wood, A. Thiessen, and G. Zimmerman, Nature (London) **239**, 139 (1972).
[2] R. Betti and O. A. Hurricane, Nat. Phys. **12**, 435 (2016).
[3] L. Rayleigh, *Scientific Papers* (Cambridge University Press, Cambridge, England, 1900).
[4] G. I. Taylor, Proc. R. Soc. Ser. A **201**, 192 (1950).
[5] R. Betti, C. D. Zhou, K. S. Anderson, J. L. Perkins, W. Theobald, and A. A. Solodov, Phys. Rev. Lett. **98**, 155001 (2007).
[6] K. S. Anderson, R. Betti, P. W. McKenty, T. J. B. Collins, M. Hohenberger, W. Theobald, R. S. Craxton, J. A. Delettrez, M. Lafon, J. A. Marozas, R. Nora, S. Skupsky, and A. Shvydky, Phys. Plasmas **20**, 056312 (2013).
[7] D. S. Montgomery, Phys. Plasmas **23**, 055601 (2016).
[8] W. Theobald *et al.*, Phys. Plasmas **15**, 056306 (2008).
[9] W. Theobald *et al.*, Phys. Plasmas **19**, 102706 (2012).
[10] S. D. Baton, M. Koenig, E. Brambrink, H. P. Schlenvoigt, C. Rousseaux, G. Debras, S. Laffite, P. Loiseau, F. Philippe, X. Ribeyre, and G. Schurtz, Phys. Rev. Lett. **108**, 195002 (2012).
[11] D. Batani *et al.*, Phys. Plasmas **21**, 032710 (2014).
[12] M. Hohenberger, W. Theobald, S. X. Hu, K. S. Anderson, R. Betti, T. R. Boehly, A. Casner, D. E. Fratanduono, M. Lafon, D. D. Meyerhofer, R. Nora, X. Ribeyre, T. C. Sangster, G. Schurtz, W. Seka, C. Stoeckl, and B. Yaakobi, Phys. Plasmas **21**, 022702 (2014).
[13] R. Nora *et al.*, Phys. Rev. Lett. **114**, 045001 (2015).
[14] W. Theobald *et al.*, Phys. Plasmas **22**, 056310 (2015).
[15] S. D. Baton, E. L. Bel, S. Brygoo, X. Ribeyre, C. Rousseaux, J. Breil, M. Koenig, D. Batani, and D. Raffestin, Phys. Plasmas **24**, 092708 (2017).
[16] G. Cristoforetti, A. Colaïtis, L. Antonelli, S. Atzeni, F. Baffigi, D. Batani, F. Barbato, G. Boutoux, R. Dudzak, P. Koester, E. Krousky, L. Labate, P. Nicolaï, O. Renner, M. Skoric, V. Tikhonchuk, and L. A. Gizzi, Europhys. Lett. **117**, 35001 (2017).
[17] G. Cristoforetti, L. Antonelli, S. Atzeni, F. Baffigi, F. Barbato, D. Batani, G. Boutoux, A. Colaitis, J. Dostal, R. Dudzak *et al.*, Phys. Plasmas **25**, 012702 (2018).
[18] W. Theobald *et al.*, Phys. Plasmas **24**, 120702 (2017).
[19] L. Antonelli *et al.*, Phys. Plasmas **26**, 112708 (2019).
[20] S. Zhang, C. M. Krauland, J. Peebles, J. Li, F. N. Beg, N. Alexander, W. Theobald, R. Betti, D. Haberberger, E. M. Campbell, R. Yan, E. Borwick, C. Ren, and M. S. Wei, Phys. Plasmas **27**, 023111 (2020).
[21] S. Baton *et al.*, High Energy Density Phys. **36**, 100796 (2020).
[22] R. S. Craxton *et al.*, Phys. Plasmas **22**, 110501 (2015).
[23] J. T. Larsen, *Cascade applied sciences, inc.* (2020).
[24] B. Bennett, J. Johnson, G. Kerley, and G. Rood, Recent developments in the Sesame equation-of-state library, Technical Report No. LA-7130, LANL, 1978.
[25] L. Jarrott, M. Wei, C. McGuffey, F. Beg, P. Nilson, C. Sorce, C. Stoeckl, W. Theoboald, H. Sawada, R. Stephens *et al.*, Rev. Sci. Instrum. **88**, 043110 (2017).
[26] C. Stoeckl, G. Fiksel, D. Guy, C. Mileham, P. Nilson, T. Sangster, M. Shoup III, and W. Theobald, Rev. Sci. Instrum. **83**, 033107 (2012).
[27] A. A. Solodov, B. Yaakobi, D. H. Edgell, R. K. Follett, J. F. Myatt, C. Sorce, and D. H. Froula, Phys. Plasmas **23**, 102707 (2016).
[28] W. Seka, B. B. Afeyan, R. Boni, L. M. Goldman, R. W. Short, K. Tanaka, and T. W. Johnston, Phys. Fluids **28**, 2570 (1985).
[29] W. Seka, D. H. Edgell, J. F. Myatt, A. V. Maximov, R. W. Short, V. N. Goncharov, and H. A. Baldis, Phys. Plasmas **16**, 052701 (2009).

[30] M. N. Rosenbluth, R. B. White, and C. S. Liu, Phys. Rev. Lett. **31**, 1190 (1973).
[31] D. W. Forslund, J. M. Kindel, and E. L. Lindman, Phys. Fluids **18**, 1002 (1975).
[32] L. Hao, W. Y. Huo, Z. Liu, J. Li, C. Zheng, and C. Ren, Nucl. Fusion **61**, 036041 (2021).
[33] M. Stoeckl and A. A. Solodov, Nucl. Instrum. Methods Phys. Res., Sect. A **931**, 162 (2019).
[34] S. Agostinelli, J. Allison, K. a. Amako, J. Apostolakis, H. Araujo, P. Arce, M. Asai, D. Axen, S. Banerjee, G. Barrand *et al.*, Nucl. Instrum. Methods Phys. Res., Sect. A **506**, 250 (2003).
[35] T. D. Arber, K. Bennett, C. S. Brady, A. Lawrence-Douglas, M. G. Ramsay, N. J. Sircombe, P. Gillies, R. G. Evans, H. Schmitz, A. R. Bell, and C. P. Ridgers, Plasma Phys. Controlled Fusion **57**, 113001 (2015).
[36] A. G. Seaton and T. D. Arber, Phys. Plasmas **27**, 082704 (2020).
[37] H. A. Rose and P. Mounaix, Phys. Plasmas **18**, 042109 (2011).
[38] R. Yan, A. V. Maximov, C. Ren, and F. S. Tsung, Phys. Rev. Lett. **103**, 175002 (2009).
[39] C. Xiao, H. Zhuo, Y. Yin, Z. Liu, C. Zheng, and X. He, Nucl. Fusion **60**, 016022 (2020).
[40] S. Atzeni, A. Schiavi, L. Antonelli, and A. Serpi, Eur. Phys. J. D **73**, 243 (2019).
[41] T. Goffrey (to be published).
[42] C. Werner, MCNP6.2 Release Notes, Technical Report No. LA-UR-18-20808, Los Alamos National Laboratory, 2018.